2019

Comparison of URANS and DES models for dynamic stall of NACA 0012 at low Reynolds number

Anshul Chandel
Iowa State University

Comparison of URANS and DES models for dynamic stall of NACA 0012 at low Reynolds number

by

Anshul Chandel

A thesis submitted to the graduate faculty

in partial fulfillment of the requirements for the degree of

MASTER OF SCIENCE

Major: Aerospace Engineering

Program of Study Committee:
Leifur Leifsson, Major Professor
Anupam Sharma
Peng Wei

Iowa State University

Ames, Iowa

2019

DEDICATION

I would like to dedicate this thesis to my parents Ramesh Kumar Chandel and Ketal Chandel who gave me their support throughout this research and in my life.

TABLE OF CONTENTS

Page

LIST OF TABLES

Page

LIST OF FIGURES

Page

ACKNOWLEDGMENTS

I would like to take this opportunity to express my thanks to those who helped me with the various aspects of conducting this research. First and foremost, Dr. Leifur Leifsson for his guidance, patience and support throughout this research and the writing of this thesis. I would also like to thank my committee members for their efforts and contributions to this work: Dr. Anupam Sharma and Dr. Peng Wei. I am also grateful to Dr. Sharma for his guidance and insights which helped me in overcoming the obstacles I had been facing throughout my research. I would additionally like to thank my fellow graduate students Vishal Raul, Xingeng Wu, Anand Amrit, Xiaosong Du and Vijigeesh Katragadda for their contribution and cooperation in this research.

NOMENCLATURE

Symbols

α	=	angle of attack, (deg)
α_o	=	mean angle of attack, (deg)
M_∞	=	free-stream Mach number
A	=	amplitude of oscillations, (deg)
Ω	=	pitch rate, (rad/s)
f	=	reduced frequency, $\frac{\omega c}{2U_\infty}$
k	=	turbulent kinetic energy, (m^2/s^2)
ω	=	specific dissipation rate, (1/s)
ϵ	=	Turbulence dissipation rate, (m^2/s^3)
U_∞	=	free-stream velocity, (m/s)
c	=	chord length of airfoil, (m)
p	=	pressure, (Pa)
p_∞	=	free-stream static pressure, (Pa)
q_∞	=	dynamic pressure (Pa), $\frac{1}{2}\rho U_\infty^2$
C_p	=	pressure coefficient, $\frac{P-P_\infty}{q_\infty}$
C_l	=	lift coefficient, $\frac{l}{q_\infty C}$
C_d	=	drag coefficient, $\frac{d}{q_\infty C}$
C_m	=	moment coefficient at quarter chord point, $\frac{m}{q_\infty C^2}$
l	=	lift force
d	=	drag force
m	=	pitching moment
dt	=	time step, (s)

ρ	=	fluid density, (kg/m^3)
u_i, u_j	=	velocity components, (m/s)
μ	=	dynamic viscosity, (kg/ms)
ν	=	kinematic viscosity, (m^2/s)
l_{DDES}	=	the length scale of the DDES model
κ	=	the Von Karman constant
d_w	=	the distance between the cell and the nearest wall
$U_{i,j}$	=	the velocity gradient, $\partial_j U_i$

Abbreviations

CFD	=	computational fluid dynamics
DDES	=	delayed detached eddy simulations
DES	=	detached eddy simulations
DSV	=	dynamic stall vortex
HAWT	=	horizontal axis wind turbines
JST	=	Jameson-Schmidt-Turkel
LES	=	large eddy simulations
LSB	=	laminar separation bubble
LU-SGS	=	lower upper symmetric Gauss-Seidel
NACA	=	National Advisory Committee for Aeronautics
SBO	=	surrogate based optimization
SST	=	shear stress transport
URANS	=	unsteady Raynolds-Averaged Navier-Stokes
VAWT	=	vertical axis wind turbines
HPC	=	high performance computing

ABSTRACT

Designing wings and rotor blades to mitigate the adverse effects of dynamic stall is of current interest. For example, unmanned air vehicles with vertical take-off and landing capability are particularly susceptible to dynamic stall as they operate entirely in the highly unsteady planetary boundary layer. The intense unsteady loads generated as the vehicle undergoes dynamic stall can lead to catastrophic failure as well as fatigue failure. A passive mechanism to mitigate dynamic stall is a desirable alternative to active control as it is simpler, robust, and economical. Innovative wing and rotor blade designs can be developed using numerical simulations and optimization techniques. The objective of this thesis is to compare and evaluate simulations of varying degrees of fidelity that can be utilized as part of designing dynamic-stall-resistant aerodynamic shapes. The unsteady Reynolds-Averaged Navier-Stokes (URANS) model is selected as the low-fidelity simulation model, whereas the detached eddy simulation is selected as high-fidelity simulation model. The unsteady flow characteristics of the NACA 0012 airfoil undergoing dynamic stall are investigated with computational fluid dynamics using the URANS equations with Menter's k-ω SST turbulence model and the detached eddy simulation (DES) at free-stream Reynolds number = 135,000, free-stream Mach number = 0.04, reduced frequency = 0.05 in a sinusoidal motion. The results are validated with published results from experiments and large eddy simulations (LES). The effectiveness of each model to capture the dynamic stall is discussed. Special emphasis is given to the various unsteady events that occur during the unsteady sinusoidal motion of an airfoil, such as laminar separation region, trailing edge flow reversal and the formation and convection of dynamic stall vortex.

CHAPTER 1. INTRODUCTION

This thesis has been modified from an article submitted to the Journal of Aircraft. The authors are Anshul Chandel, Vishal Rao, Xingeng Wu, Leifur Leifsson and Anupam Sharma. Anshul Chandel is the primary author and was responsible for the overall comparison of models and the dissemination of this research work. Anshul Chandel and Vishal Rao were also responsible for the unsteady Reynolds-Averaged Navier-Stokes (URANS) simulations and investigations. Xingeng Wu was responsible for the detached eddy simulations (DES). This research was conducted under the guidance and oversight of Dr. Leifur Leifsson and Dr. Anupam Sharma.

1.1 Motivation

For years, researchers have been intrigued by dynamic stall and its effects on engineering devices such as rotor blades for helicopters [2, 3], wind turbines [4, 5], and unmanned aerial vehicles. In particular, numerous works have investigated the effects of dynamic stall in unsteady flows and its benefits in effectively delaying stall on wings. Dynamic stall occurs when an airfoil or a wing undergoes a large rapid change in angle of attack in an unsteady aerodynamic environment. A rapid increase in the angle of attack results in the formation of a vortex on the suction side of the airfoil which detaches from the leading edge, travels downstream and sheds into the wake. This is called a dynamic stall vortex (DSV). The velocity induced by this vortex leads to the variation in the lift and drag forces and the moments acting on the wing. Due to the DSV formation, there is an additional suction on the upper surface which gives an increase in lift leading to higher maximum lift attained by the airfoil than in the steady state motion. As DSV convects past the trailing edge, the flow becomes fully separated with a steep decline in the lift force and the airfoil/wing experiences stall. This "stall" angle of attack is considerably higher than the steady-state stall angle. This delay in stall is a critical point of interest for researchers in the field of unsteady aerodynamics.

As the angle of attack is reduced, the flow starts reattaching itself from the leading edge to the trailing edge. There is a critical need to accurately model the dynamic stall event and design the aerodynamic devices to mitigate its effects. The overall objective of this work is to evaluate and compare simulation models of the dynamic stall for airfoil shapes undergoing unsteady motion.

1.2 Literature Review

The initial observation of dynamic stall was first made in helicopters when the researchers observed a higher lift produced by the rotor blades than the steady state flow in the retreating blade condition. This extra lift is due to the formation of a DSV on the leading edge of the airfoil and was first observed by Ham *et al.* [2]. This DSV is a critical feature of the dynamic stall problem which was shown by numerous experimental and computational investigations [6–8]. Majority of the experimental studies in the 70's and 80's were focused on the retreating blade stall in the high-speed forward flight of helicopters [3, 9, 10]. Many other researchers also performed experimental studies during that time, which were focused on the dynamic stall behavior on oscillating airfoils [11–13]. A review of dynamic stall on the NACA 0012 airfoil was given by McAlister *et al.* [12]. A detailed overview on dynamic stall characteristics and the effect of various parameters such as pitching frequency, airfoil shape and Reynolds number on dynamic stall was given by Carr [14]. During that period, due to the computational limitations to simulate the unsteady characteristics of dynamic stall, a number of researchers focused on developing semi-empirical models to represent the physical processes by using linear or non-linear equations to simulate the unsteady aerodynamic flow. Some of these models used to predict dynamic stall in helicopter rotor blades can be found in [3, 15–17]. These models used the airfoil loads measurements from both steady and unsteady experiments to predict the unsteady dynamic stall characteristics.

In the recent years, significant progress has been made in simulating the unsteady flow characteristics of dynamic stall using computational fluid dynamics (CFD) models with considerable accuracy. Most of these models are based on the numerical solution of the Navier Stokes equations, which has been reasonably successful in modeling dynamic stall. Most of these models are used

to simulate the flow at relatively low Reynolds numbers (around 10^5) which makes them useful applications such as vertical axis wind turbines (VAWT) or horizontal axis wind turbines (HAWT), with a much research being done in this area [4, 5, 18, 19].

Lately, the focus has been on computational investigations which provide insights into the physical mechanism of dynamic stall [20–22]. The broadly used computational methods for simulating unsteady flows are direct numerical simulation (DNS), large eddy simulations (LES), detached eddy simulations (DES) and unsteady Reynolds averaged Navier Stokes (URANS) methods. DNS is the most computationally advanced method which resolves even the smallest scales in the flow but the computing resources required for this method are very high. LES is a widely used computational method which computes time-varying flow and models sub-grid-scale motions but the computational resources required to model unsteady simulations are still high for high Reynolds number problems [19, 23]. URANS is a reasonably accurate method to model dynamic stall simulations and the computational cost is lower than other computational methods [24–26]. DES [27] is a recently developed computational method which combines URANS and LES by using LES in the far field and URANS in the boundary layer region of the airfoil. A comprehensive study of DES models has been performed by Deck [28] and a DES/LES comparison for unsteady turbulent flows was carried out by Basu *et al.* [29]. An overview of the comparison of URANS, DES and LES is given by Celik *et al.* [30] and Zhong *et al.* [31].

The simulation-based design and optimization of aerodynamic surfaces to mitigate dynamic stall effects will require fluid flow simulations that can capture the relevant unsteady physics. Furthermore, having fast simulation models is critical since numerical optimization techniques, typically, require repetitive and iterative evaluations. Gradient-based search with adjoint sensitivities [32–36] is the current state of the art approach for solving aerodynamic shape optimization problems. The major advantage of this approach is that the gradients of the objective and constraints can be estimated based on the primal flow simulation and one adjoint simulation. The cost of one adjoint evaluation is comparable to one flow evaluation [33–36]. Consequently, the gradient-based aerodynamic shape optimization problem is, nearly, independent of the number of design variables. The

disadvantage, however, is that the adjoint sensitivity approaches have been developed for RANS and URANS and are not available for methods of higher fidelity.

Surrogate-based optimization (SBO) [37–39] is another way to alleviate the computational cost. The key idea behind reducing the computational effort in SBO is to replace the direct handling of the expensive simulation by iterative construction and re-optimization of their fast replacements, referred to as surrogates. The number of evaluations depends on the method used to construct the surrogate model. Approximation-based models [37,38] are obtained by approximating sampled simulation data. The downside of these modeling approaches is that the setup cost (specifically, the cost of acquiring the training data) grows quickly with the number and the ranges of the design variables.

Multifidelity models [39–48] are constructed using a suitably corrected physics-based low-fidelity simulation models (URANS), which is a less accurate but a computationally cheaper representation of the high-fidelity simulation (such as DES). The most important advantage of multifidelity surrogates over approximation-based ones is their good generalization capability which comes from the knowledge about the system of interest embedded within the underlying low-fidelity simulation model. Consequently, a limited amount of high-fidelity data is needed to ensure a good predictive power of the surrogate. Often only one high-fidelity simulation per algorithm iteration is needed. Thus, SBO with multifidelity models can be a promising option for dealing with shape optimization of dynamic-stall-resistant aerodynamic surfaces. In particular, the approach provides a way of utilizing the range of available simulations.

1.3 Research Objectives

In this thesis, the URANS and DES methods are selected for the dynamic stall simulations to be evaluated and compared with the intent of using those as part of multi-fidelity modeling. Here, URANS is considered the low-fidelity model and DES the high-fidelity one. The objective is to evaluate and compare the models in terms of the airfoil characteristic parameters (the lift, drag, pitching moment, pressure, and skin friction coefficients), as well as in terms of the features of

the predicted flow fields (the velocity, pressure, and vorticity fields). The computational experiments with the simulation models are compared with the LES results of Yusik *et al.* [18] and the experimental results from the wind tunnel data obtained by Lee and Gerontakos [49]. The experimental study by Lee and Gerontakos [49] is comprehensive with a wide variety of cases with varying reduced frequency. They conducted extensive wind tunnel tests and measured the results through multi-element hot film sensor array signals and pressure transducers on the suction side. In order to ensure two-dimensional uniformity with the three-dimensional experiments, they used end-plates with minimum spacing between the end-plates and the airfoil to reduce the amount of flow through the gaps. The results were averaged over one hundred pitching cycles for all the cases. The dynamic stall cases are generally categorized as attached flow (low angle of attack, no separation), light stall (small angle of attack, small separation region), and deep stall (large angle of attack, large separation). A similar study was performed by Wang *et al.* [21] with a comparison of various turbulence models and URANS and DES with a higher reduced frequency value of 0.1.

1.4 Thesis Outline

The outline of the remainder of this thesis is as follows. Chapter 2 provides a background of dynamic stall and the various events associated with unsteady aerodynamics. In Chapter 3, computational methods are described. Chapter 4 presents the results observed from the unsteady simulations along with the comparison in prediction of dynamic stall by various models. Chapter 5 concludes the thesis.

CHAPTER 2. BACKGROUND

Dynamic stall is associated with a series of unsteady events as the airfoil undergoes a pitching or plunging motion. Figure 2.1 depicts conceptual sketches of the airfoil and the flow structure at various stages during the pitching cycle. Figure 2.2 shows these events on sketches of the lift and moment hysteresis loops for one pitch cycle. In static conditions, the lift curve generally goes up to the static stall point which is the peak of the static lift curve (static-C_{lmax}) shown as point 1 as shown in Fig. 2.2. In the case of unsteady motion, the change in angle of attack is rapid enough such that the flow stays attached to the airfoil surface even beyond the static stall point. This is attributed to various effects such as apparent camber, boundary layer lag, and most importantly, induced lift by the dynamic stall vortex. As the angle of attack of the airfoil increases, the flow is characterized by a laminar separation bubble (LSB) on the upper surface near the leading edge and the upstream movement of flow reversal from the trailing edge towards the leading edge. The LSB is formed due to the laminar flow being exposed to an adverse pressure gradient. The flow transitions to turbulence in the shear layer and the turbulent flow reattaches itself to the airfoil while trapping a recirculating flow region which is called an LSB [50].

As the airfoil is in the upstroke, the increasing angle of attack leads to the shortening of the LSB and eventually bursting of the LSB. At this point, depicted by point 2 in Fig. 2.2b, the airfoil experiences a sharp increase in nose-down pitching moment. This point is also referred to as moment stall. This leads to a large disturbance characterized by the formation of a DSV. This highly energetic DSV grows in size and travels and eventually detaches from the airfoil surface. The DSV causes an increase in lift and once the maximum lift is attained, it drops down rapidly and the dynamic stall occurs, shown as point 3 in the figures. After this point, as the DSV detaches from the surface, the lift drops fully separated flow is observed over the suction surface of the airfoil (point 4). During this post-stall region, the airfoil starts the downward stroke and the formation

of a secondary vortex occurs which leads to a slight increase in lift marked by point 5 in Fig. 2.1. As the airfoil is in the down-stroke, the flow starts reattaching to the airfoil from the front to the rear (point 6); complete flow reattachment at (point 7).

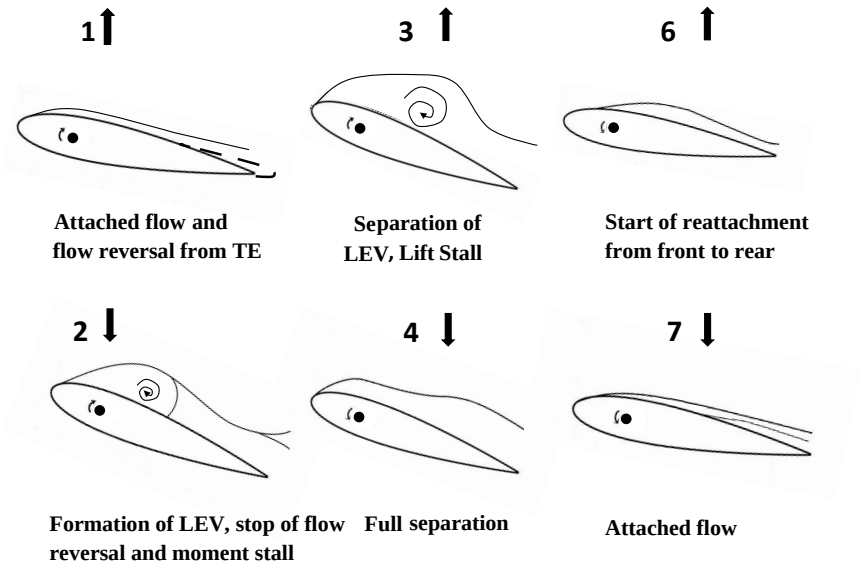

Figure 2.1: Dynamic stall events for the flow an airfoil. The numbers refer to the events in Fig. 2.2

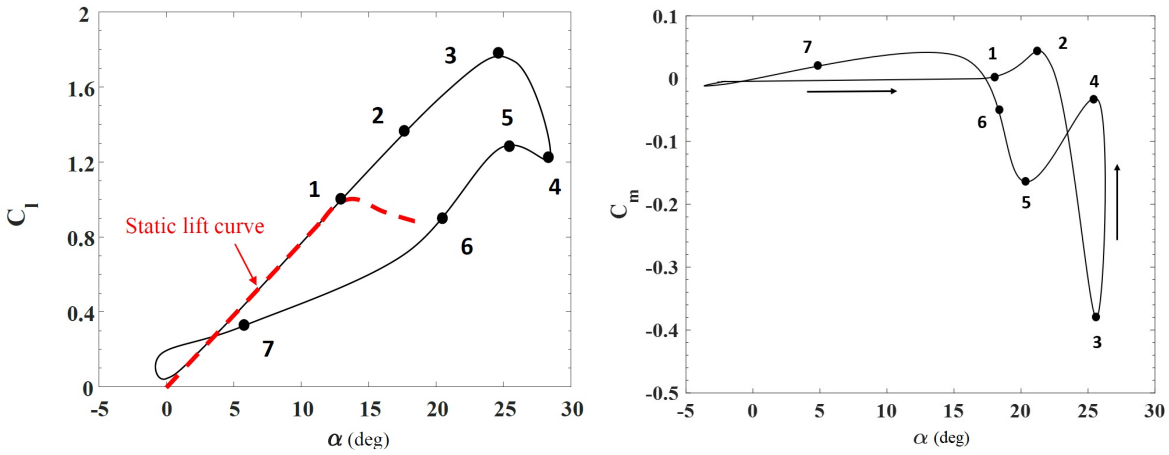

(a) (b)

Figure 2.2: Effects of dynamic stall events in Fig. 2.1 on lift and pitching moment coefficients

CHAPTER 3. METHODS

In this section, we describe the problem and the methods used to model dynamic stall with the description of governing equations and the computational grids used for each model.

3.1 Problem Definition

The airfoil undergoes a sinusoidal pitching motion about the quarter chord point as shown in Fig 3.1. The airfoil experiences a normal force (C_n) with x,y being fixed with the ground and the airfoil oscillates in the positive y-direction. The airfoil also experiences a positive pitching moment (C_m) when the airfoil pitches in the nose-up direction. The pitching motion occurs in a sinusoidal manner which is governed by the equation

$$\alpha = \alpha_o + Asin\Omega t \tag{3.1}$$

The Reynolds number is 135,000, Mach is 0.04 and a mean angle of attack α_o is 10° with respect to the airfoil. The amplitude of the oscillations (A) is 15° and the pitch rate of the motion (Ω) is 1.36 rad/s, which is based on the reduced frequency (f) given by

$$f = \frac{\Omega c}{2U_\infty} \tag{3.2}$$

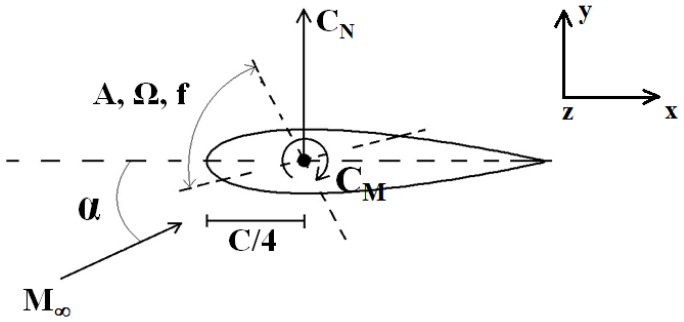

Figure 3.1: Forces and moments acting on an airfoil in a pitching motion

where the chord length (c) is 1 m and the free-stream velocity (U_∞) = 13.6 m/s. The reduced frequency is chosen as 0.05 for the present study.

3.2 Unsteady RANS Simulation Model

The URANS method of CFD simulations considers the turbulence effect on the flow by solving the Reynolds-Averaged Navier-Stokes equations using appropriate models for turbulent quantities [51]. The most widely used eddy viscosity model assumes the direct proportionality of turbulent stress with the mean rate of strain. The turbulent transport equations are then used to determine the eddy viscosity. These equations generally involve the turbulent kinetic energy (k) and another quantity such as specific dissipation rate (ω) or rate of dissipation of turbulent energy (ϵ). This is why this model is also sometimes called a two-equation model. In this work, Menter's shear stress transport k-ω model is used for the unsteady RANS simulations [52], which is a two-equation model combining the traditional k-ω and k-ϵ models. A computational investigation by Wang *et al.* [24] shows that the SST k-ω model predicts dynamic stall with higher accuracy than the standard k-ω model.

3.2.1 Governing Equations

RANS equations involve Reynolds averaging to decompose the flow into averaged and fluctuating components. This process is called Reynolds decomposition. The most general aspect of Reynolds averaging is ensemble averaging which is both time and space dependent and can be described as an average of N number of identical experiments. After the process of decomposition the flow can be divided into averaged (ensemble) and the fluctuating components as

$$\begin{aligned} u_i &= U_i + u_i, \\ p &= P + p, \\ T_{ij}^{(\nu)} &= T_{ij}^{(\nu)} + \tau_{ij}^{(\nu)}, \end{aligned} \tag{3.3}$$

where U_i, P and $T_{ij}^{(\nu)}$ are the averaged components and u_i, p and $\tau_{ij}^{(\nu)}$ are the fluctuating components. After inserting these decomposed expressions into the instantaneous equations and averaging, we get the RANS equations

$$\rho\left(\frac{\partial U_i}{\partial t}+U_j\frac{\partial U_i}{\partial x_j}\right)=-\frac{\partial P}{\partial x_i}+\frac{\partial T_{ij}^{(\nu)}}{\partial x_j}-\frac{\partial}{\partial x_j}\left(\rho\left(u_iu_j\right)\right), \tag{3.4}$$

where the last term is the contribution of the fluctuating quantities which acts as a stress on the mean fluid motion. Hence, this term is called the Reynolds stress tensor and it corresponds contribution of the unresolved on the resolved mean flow.

Also, the URANS equations are called unsteady RANS equations because of the retention of the $\frac{\partial U_i}{\partial t}$ term in the computation. Also, as the ensemble averaged components are time dependent too, the URANS results are unsteady but we take the results only for the time-averaged flow. Hence, the results from URANS are decomposed into the time averaged component, U_i, turbulent fluctuation, u_i and a resolved fluctuation, u_i' in the form of $u_i = U_i + u_i + u_i'$.

3.2.2 CFD setup

The URANS simulations were performed using the Stanford University Unstructured (SU2) [53] solver and the k-ω SST turbulence model [52]. The Green Gauss numerical method is chosen for gradient calculation to ensure the accuracy and robustness of the CFD method and satisfy the geometrical monotonicity condition [54]. The CFL number is set to 4. The flexible generalized minimal residual method is chosen as the non-symmetric linear equations solver for the implicit formulation [55]. The nonlinear lower upper symmetric Gauss-Seidel (LU-SGS) algorithm [56] is used to solve the nonlinear algebraic systems related to implicit time discretizations. Jameson-Schmidt-Turkel (JST) scheme [57] is used as the convective numerical method for convergence acceleration. Venkatakrishnan slope limiter [58] is used to reduce numerical dissipation in smooth regions. Euler implicit scheme is used for time discretization. The 2nd order dual time stepping scheme [59] is used for the unsteady simulations. Free-stream turbulence intensity is set at 0.08% which is the same as in the experimental work by Lee *et al.* [49].

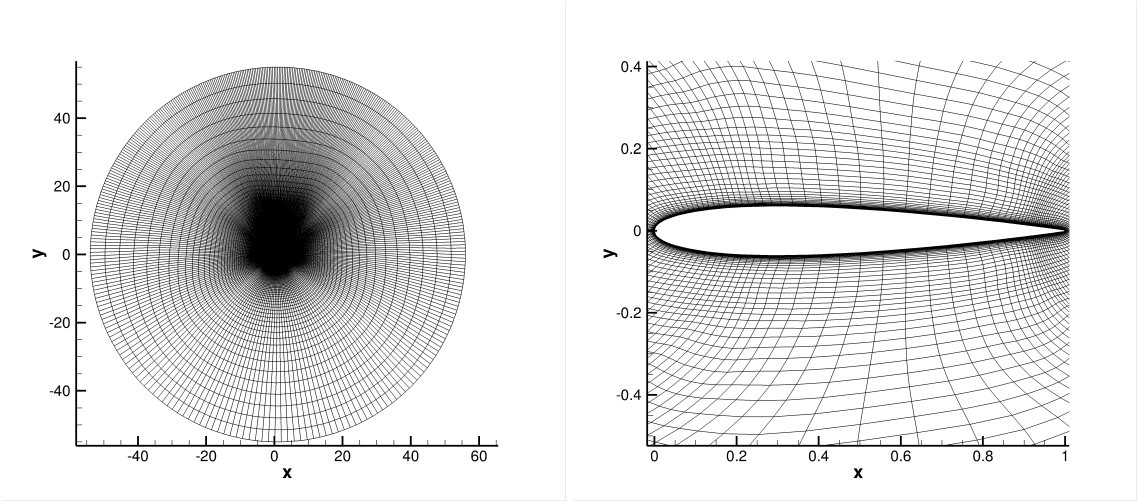

(a) (b)

Figure 3.2: A sample computational grid used in URANS simulations showing (a) the farfield and (b) close-up of airfoil

3.2.3 Computational Grid

A structured multi-block O-grid was made in GridPro [60] for the URANS simulation. GridPro is an open source meshing software which uses automatic topology generation [60] that provides high level of flexibility to create blocks so that a large number of blocks can be created quickly. The grid is created with higher number of blocks near the geometry such that the boundary layer region has a higher mesh density than the far-field region. Mesh orthogonality is improved close to the airfoil surface. The nesting feature provided by Gridpro is used in this work to capture the airfoil wake without increasing the overall cell count and increasing the aspect ratio by rapid coarsening of the mesh in the normal direction away from the airfoil surface. The far-field boundary is made with a 55 chord radius. The chord length of the airfoil is set to 1 m.

A grid study is performed using four different mesh sizes with the coarsest mesh having 10,000 cells and the finest having 500,000 cells with the first layer thickness of 1.0E-6. With the Reynolds number as 135,000 and Mach number of 0.04, the first cell thickness for all the mesh sizes is assigned to keep the y^+ value below 1 and the growth ratio within the boundary layer region as 1.2. This y^+ value is adequate for the flow conditions and the growth ratio is within the range for sufficient

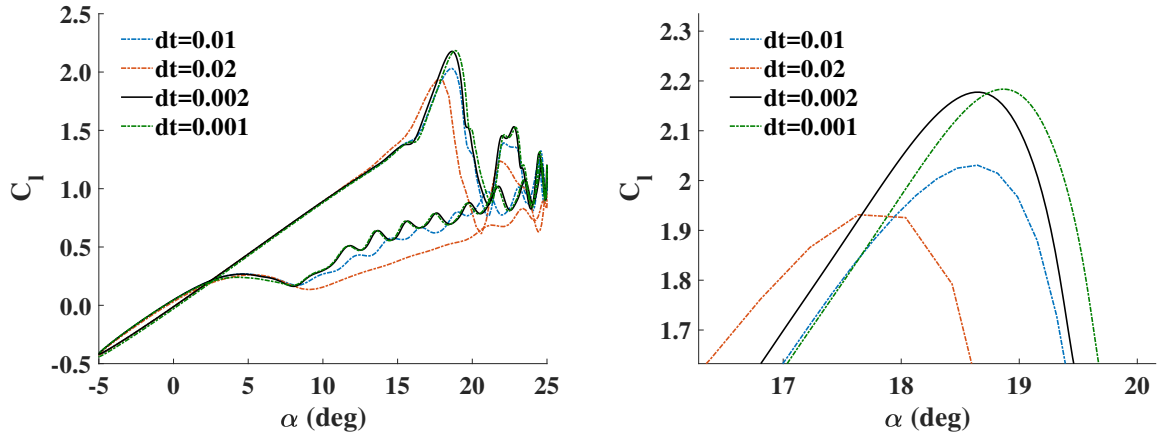

Figure 3.3: Time step study for the URANS simulations: (a) lift curves at different time step values, and (b) zoom-in of area around the peak values

log-layer resolution for RANS calculations as proposed by Spalart [61]. The far-field and boundary layer region of the mesh are shown in the Figs. 3.2a and 3.2b, respectively.

A time step study is conducted by running the URANS simulations for four different time step size (dt) values. The parameters are kept the same for all simulations and the results are compared as shown in Fig. 3.3. The time step study is necessary to accurately capture the transient flow physics. Whereas, a lower dt value which can capture the flow physics accurately will increase the time required for the simulations. After a careful comparison of results from Fig. 3.3 and keeping in mind the offset of flow accuracy and time duration, the dt value of 0.002 is chosen for the flow simulations.

3.2.4 Steady RANS Simulation

For the grid refinement study, the static case is chosen as angle of attack 6°, with Reynolds number 170,000. The angle of attack of 6° is chosen because the main goal is to capture boundary layer transition. The results are compared with the experimental data from the National Advisory Committee on Aeronautics Report no. 586 experimental study [1]. The Mach number for the

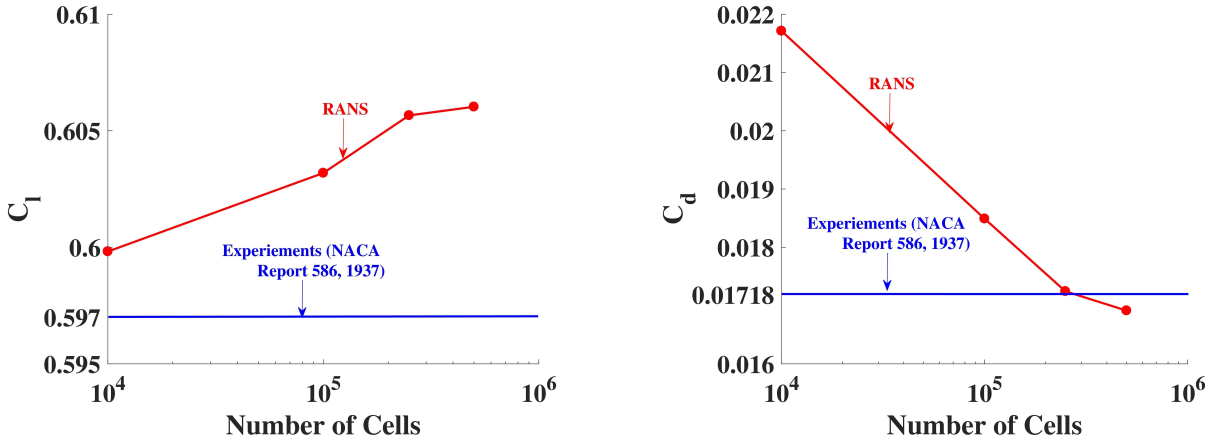

Figure 3.4: Grid independence study for the steady RANS simulations showing the variation of (a) the lift coefficient and (b) the drag coefficient with the number of mesh cells. Experimental data is shown in [1]

static case is 0.04 and the turbulence intensity is 0.08%. The results for the grid independence study are plotted in Fig. 3.4

From the results of the grid study, the grid for the fine mesh is chosen as the one with 250,000 cells. This decision is based on the observation that the results of the 500,000 cells grid and the 250,000 cells grid are comparable, whereas the time duration of the simulation for the 250,000 cells grid is far lesser than the other one. The pressure coefficient (C_p) distributions from steady RANS and DES are compared with XFOIL predictions as shown on Fig. 3.6. XFOIL is a vortex panel method code and uses the e^N theory to capture BL transitions; the theory states that the disturbance in linearized boundary layer equations grows e^N times before passing to turbulence. The simulations are performed with two N_{crit} parameter values. N_{crit} is the log of the amplification factor of the most amplified wave which initiates the transition. N_{crit} determines the turbulence level, that is, if N_{crit} is 1, large amount of disturbance is present in the flow. $N_{crit} = 9$ is the standard and very commonly used. From Fig. 3.6a, we can infer that the overall agreement of the RANS and DES models is good with the XFOIL predictions except for the difference in prediction of the turbulent transition region. In Fig. 3.6b, we see that the RANS model under predicts the location of the transition region compared to the XFOIL predictions, whereas the DES model does

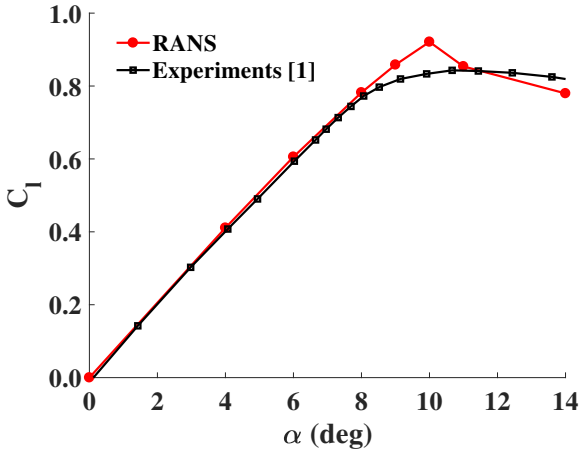

Figure 3.5: A comparison of lift curves obtained from steady RANS simulations and experimental data [1].

not capture the transition region but is in overall agreement with other models. This is because RANS in the DES model does not have a transition model in it which is why it doesn't capture the transition region.

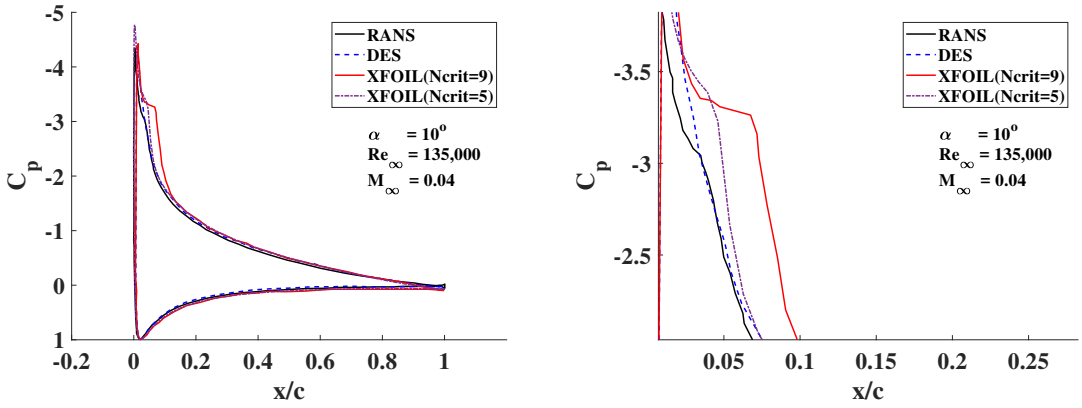

(a) (b)

Figure 3.6: Comparison of the steady RANS, steady DES and XFOIL (Ncrit = 5 and 9) models (a) pressure coefficient distributions and (b) a close-up view of the same showing the turbulent transition region

3.3 Detached Eddy Simulation Model

Detached eddy simulation (DES) was first introduced in 1997 [62]. Since then, it has been widely used in many high Reynolds number applications. DES is a hybrid RANS-LES turbulence model that uses RANS model formulations to predict the attached flow close to solid boundaries and switch to LES model to resolve large eddies in the separated or detached flow region. Compared to the LES model, DES acts like a RANS model near wall boundaries where much coarser grids can be used. Thus, DES can significantly reduce the computational expense of high Reynolds number simulations.

3.3.1 Governing Equations

The three dimensional DES simulation in this study is performed with the $k-\omega$ DDES model [63]. In this model, the $k-\omega$ turbulence closure model is used for the RANS branch to calculate the eddy viscosity (ν_T) in the LES branch, which is defined by

$$\nu_T = l^2_{DDES}\,\omega, \tag{3.5}$$

where, l_{DDES} is written as

$$l_{DDES} = l_{RANS} - f_d\,\max(0, l_{RANS} - l_{LES}), \tag{3.6}$$

where $l_{RANS} = \sqrt{k}/\omega$ and $l_{LES} = C_{DES}\triangle$, which are the length scales of the RANS and LES branches respectively, with C_{DES} being a constant and $\triangle = f_d\,V^{1/3} + (1-f_d)\times\max(dx, dy, dz)$. In (3.6), f_d is a shielding function, written as

$$f_d = 1 - \tanh\{(8\,r_d)^3\}, \tag{3.7}$$

where $r_d = \frac{k/\omega+\nu}{\kappa^2 d_w^2\sqrt{U_{i,j}U_{i,j}}}$. Equation 3.6 shows how, the DDES length scale l_{DDES} can switch between l_{RANS} and l_{LES}, indicating how the DDES model switches between RANS and LES.

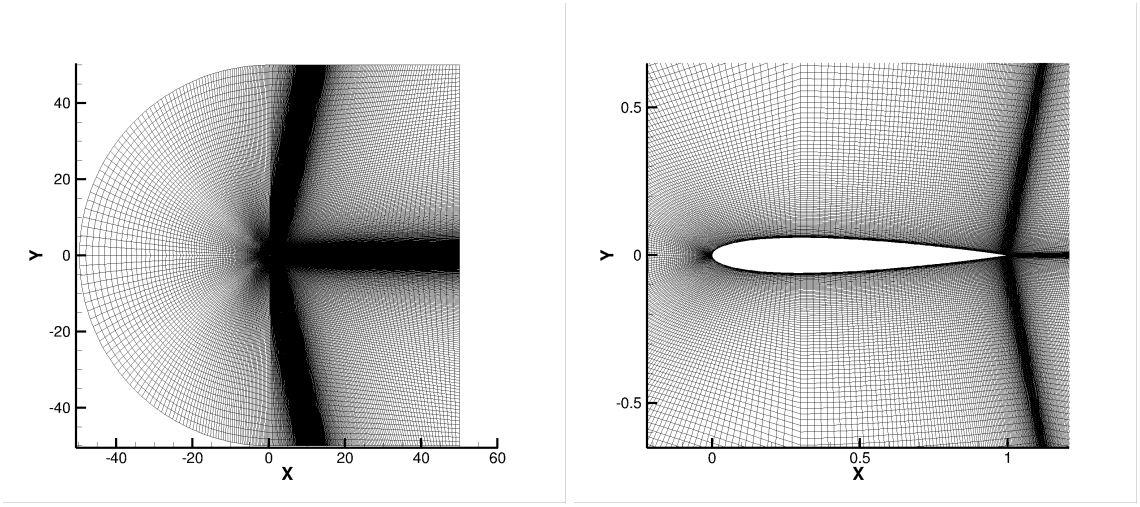

(a) (b)

Figure 3.7: A cross-sectional view of the computational grid for DDES Simulation showing (a) the overall domain and (b) close-up of the airfoil

In the RANS branch ($f_d = 0$ or $f_d = 1 \,\&\, l_{RANS} < l_{LES}$), the eddy viscosity is written as $\nu_T = l_{RANS}^2 \omega = k^2/\omega$, where k and ω are calculated based on the transport equations as

$$\frac{Dk}{Dt} = 2\nu_T |S|^2 - C_\mu k\omega + \partial_j[(\nu + \sigma_k \nu_T)\partial_j k], \tag{3.8}$$

$$\frac{D\omega}{Dt} = 2C_{\omega 1}|S|^2 - C_{\omega 2}\omega^2 + \partial_j[(\nu + \sigma_\omega \nu_T)\partial_j \omega]. \tag{3.9}$$

In the LES branch ($f_d = 1 \,\&\, l_{RANS} > l_{LES}$), the eddy viscosity is written as $\nu_T = l_{LES}^2 \omega = (C_{DES}\triangle)^2\omega$, which is close to the eddy viscosity in the Smagorinsky model, written as $\nu_s = (C_s\triangle)^2|S|$ [63].

3.3.2 Computational Grids

A three-dimensional C-grid was created for the DES simulation in this study. A cross-sectional view of the overall computational domain and a close-up of the airfoil are shown in Fig. 3.7. The NACA-0012 airfoil is located in the center of the computational domain. The first cell height is chosen to ensure $y^+ < 1$ over the airfoil surface. The outer boundary of the domain is at a distance

of around $50 \times c$ away from the airfoil surface and the span dimension of the airfoil is $0.25 \times c$. The free stream boundary condition is applied on the outer boundary, while periodic boundary conditions are applied in the span direction. The entire computational grid consists of 3.2 M cells with 19 cells in the span direction.

CHAPTER 4. RESULTS

In this section, the results and observations from the DES and URANS simulations are presented. An overview of the simulations is given in the first subsection followed by observations on the dynamic stall events. In the third subsection, the results from all the models are compared.

4.1 Description

Both 2-D and 3-D dynamic simulations are performed using a solid body motion of the grid with the oncoming flow fixed at angle of 10° with respect to the x-axis. The grid undergoes a sinusoidal pitching cycle about the airfoil quarter chord point with the amplitude of the oscillation being 15° and the oscillating frequency of 1.36 rad/s. As a result of this setup, the airfoil oscillates between −5° (lowest point of the pitching cycle) and 25° (highest point of the pitching cycle). The URANS simulations are performed for three cycles and the results from the third cycle are used to eliminate the effect of transients. The time step is selected as 0.002 sec from the time-step study (described in the section 3.C.4) with the total simulation time of 15.2 sec required for 3 cycles. The number of internal iterations is selected as 10,000 with average convergence observed at 4000 iterations. The DES simulations are only performed for two cycles of pitching motion because they are very expensive and time-consuming (simulation time = 350,000 CPU hours for 2 cycles). The aerodynamic forces and moment for the DES simulations are averaged over two cycles. Other simulated results are instantaneous and not averaged.

4.2 Dynamic Stall Events

The lift and pitching moment hysteresis curves observed in the oscillating airfoil cycle with URANS and DES simulations are shown in the Fig. 4.1. The important events are shown with black dots and are numbered from 1 to 8 on the URANS curves. Similar events are also observed in the DES

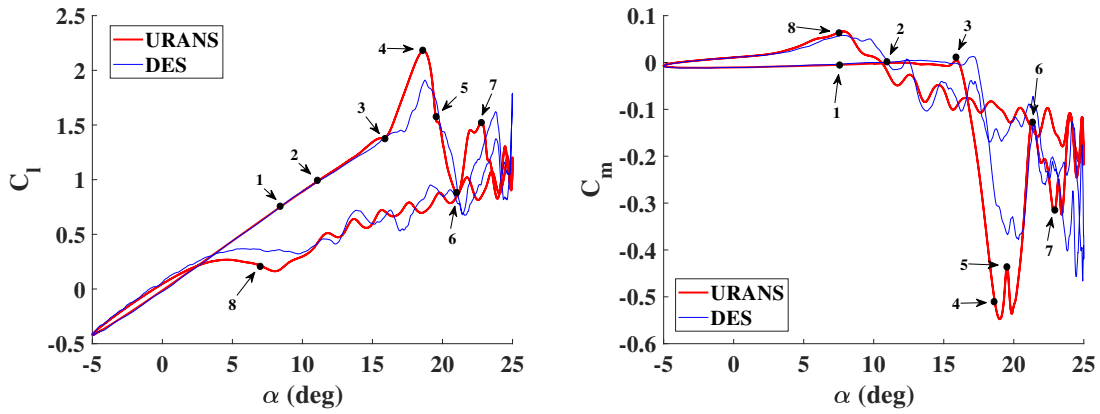

(a) (b)

Figure 4.1: Dynamic stall events shown on (a) the lift curve and (b) the pitching moment curve.

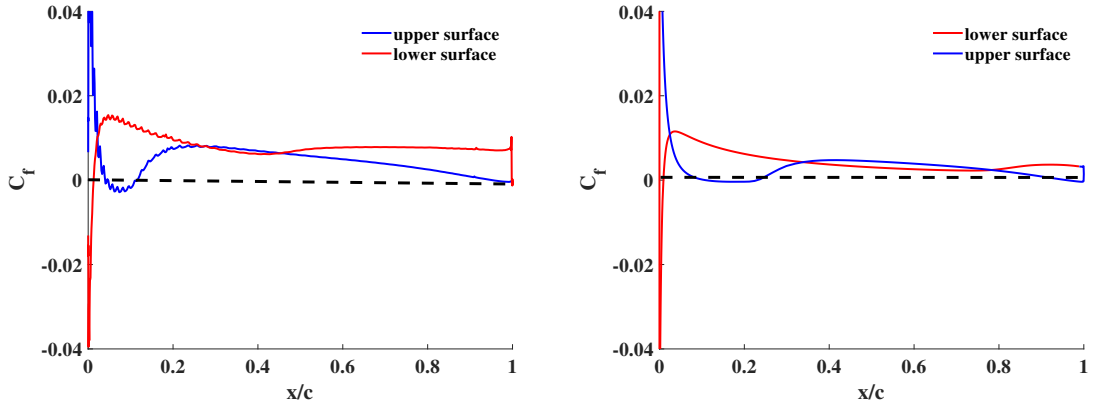

(a) (b)

Figure 4.2: Coefficient of friction curve at (a) $\alpha = 8.35° \uparrow$ for URANS and (b) $\alpha = 8.10° \uparrow$ for DES.

simulation. Each point in this section represents an event in the airfoil pitching cycle. The details of these events and the corresponding angles of attack observed in the URANS and DES simulations are discussed in this section. The upward arrow $\uparrow$ represents the upstroke of the pitching cycle (pitch-up motion), whereas the downward arrow $\downarrow$ represents the down-stroke (pitch-down motion).

Observations on the dynamic stall events are following:

1. Formation of laminar separation region ($\alpha = 8.35°$ for URANS and $\alpha = 8.10°$ for DES) $\uparrow$:

   The airfoil upstroke pitching cycle starts from -5° angle of attack. As the angle of attack increases, the lift and drag values increase steadily without any sign of flow separation until α

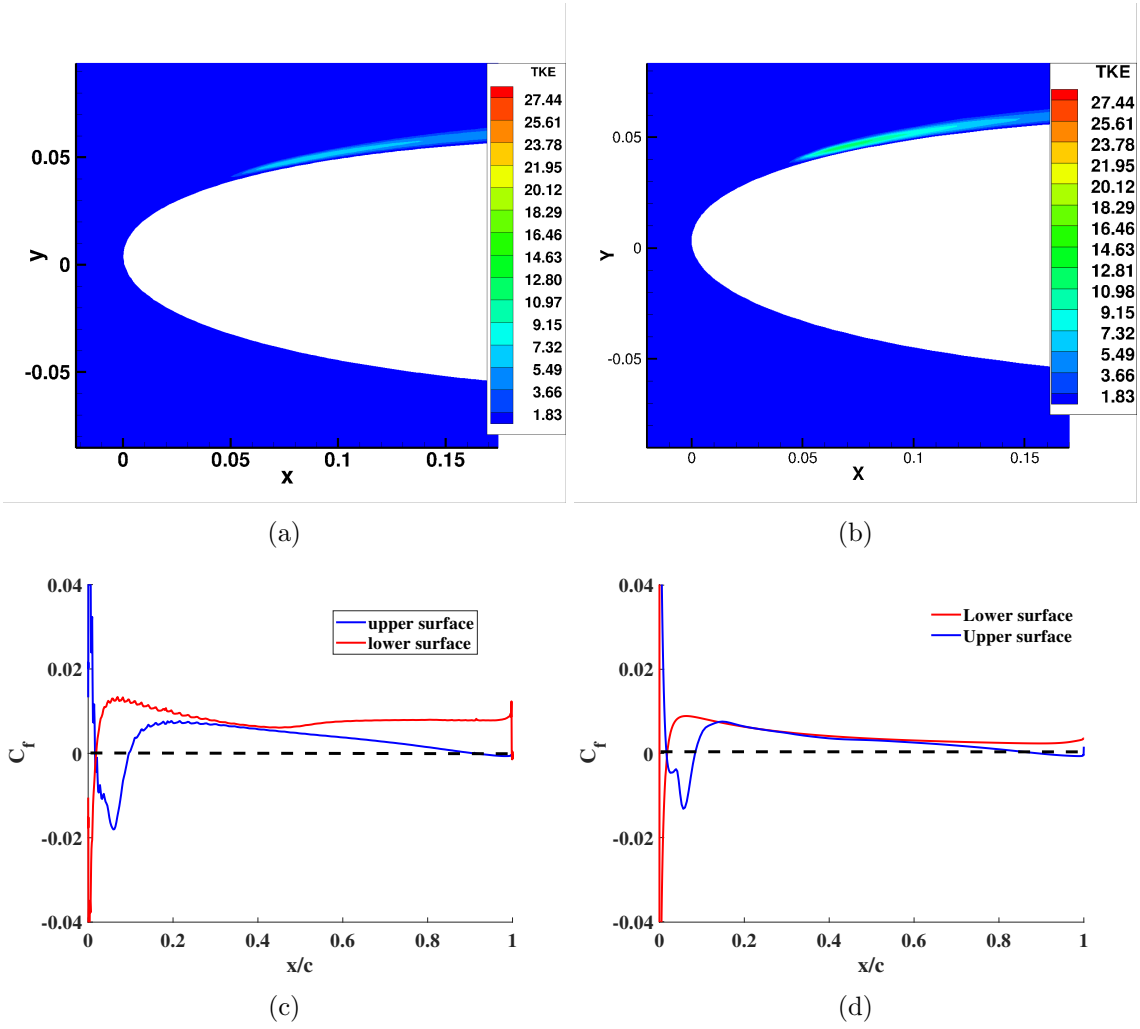

Figure 4.3: Contours for the URANS model at 11° ↑ of (a) vorticity in z-direction and (c) the C_f curve. Contours for the DES model at 10.87° ↑ of (b) vorticity in z-direction and (d) the C_f curve.

= 8.35°. At $\alpha = 8.35°$, a thin layer of laminar separation region is observed near the leading edge between 0.05c and 0.1c. This region is characterized by the negative C_f in Fig. 4.2. Span averaging is used in DES to get these C_f plots. After this region, the flow transitions into a turbulent flow. This laminar separation region moves towards the leading edge until point 2 is reached in Fig.4.1.

2. Onset of flow reversal and initial formation of DSV ($\alpha_{SS} = 10.98°$ for URANS and $\alpha_{SS} = 10.87°$ for DES) ↑ : At this point, the laminar separation region reaches the leading edge and

the initial formation of the DSV is observed between 0.02c and 0.15c as shown in Fig. 4.3. Contour plots of turbulent kinetic energy are shown in Figs. 4.3a and 4.3b. The region of high turbulent kinetic energy in these plots indicates the location of the DSV.

Interestingly, the beginning of trailing edge flow reversal is also observed in both URANS (10.98°) and DES (10.87°) simulations as shown by negative values of C_f near the trailing edge in Figs. 4.3c and 4.3d. This angle happens to be the static stall angle for the NACA 0012 airfoil as seen in the static simulation (section 2.C.4).

3. End of upward spread of trailing edge flow reversal (α (URANS) = 15.91° and α (DES) = 17.06°) $\uparrow$: As the airfoil continues in upstroke, the DSV grows in size and intensity. This can be seen from the low pressure region observed in the C_p contour plots (Fig. 4.4a and 4.4b). The location of the DSV is represented by a region of negative C_f as shown in Figs. 4.4e and 4.4f. It can also be observed that the growth in the size and intensity of the DSV is clear in both the URANS simulation and in the DES simulation. This can be seen by the comparing the negative z-vorticity region observed in URANS and DES simulation (Fig. 4.4c 4.4d). The flow reversal at the trailing edge also travels upstream from the trailing edge towards the leading edge over the surface of the airfoil as can be seen by the negative C_f region near the trailing edge in the Figs. 4.4e and 4.4f. This is also the moment stall point as shown in Fig. 4.1b. The DSV detaches from the leading edge and travels over the airfoil leading to the increase in the lift coefficient and rapid decrease in moment coefficient once it crosses the quarter chord point. The moment stall point is determined by fixing an arbitrary criterion of 5% i.e. the point which satisfies the slope $\frac{\partial C_m}{\partial \alpha} < 0.05$ on the pitching moment coefficient curve in Fig. 4.1b near the region when positive pitching moment starts to decrease rapidly.

4. Dynamic stall (α_{DS} (URANS) = 18.66° and α_{DS} (DES) = 19.13°) $\uparrow$: After moment stall point, the DSV continues to grow in size and convects downstream over the upper surface of the airfoil. This is the major reason for the large variations observed in C_l and C_m values between points 3 and 4 in Fig. 4.1. In Fig. 4.1a, the lift-curve slope increases after

point 3, due to the rapid growth of the DSV. Similarly, in Fig. 4.1b, a sudden drop in the pitching moment coefficient is observed. This is mainly due to the convection of DSV and the downstream movement of cumulative lift force. This induces a nose-down pitching moment on the airfoil. The location of this DSV can be seen from the C_p contours (Fig. 4.5a and 4.5b) and C_f plots (Fig. 4.5e and 4.5f). The core of the DSV is observed to be around 0.7c in both DES and URANS simulation by observing the C_p contour plots. The location of the most negative value of C_f plots also corresponds to the location of the core of the DSV.

The rearward convection of this energetic DSV continues till point 4 (Fig. 4.1a), where it spreads over almost the entire airfoil surface as shown in Figs. 4.5c and 4.5d. The DES shows some extra eddies (Fig. 4.5d) which are not observed in URANS (Fig. 4.5c) which maybe because DES is stochastic in nature. If an ensemble average of the results is taken over time, it becomes more deterministic in nature and we will see a similar image as obtained from URANS simulation (4.5c).

At this point, the airfoil achieves the maximum lift coefficient as shown in Fig. 4.1a by point 4. After this point, the DSV begins to detach from the airfoil surface, which leads to a rapid drop in lift coefficient. This event is called dynamic stall. At this point the C_m curve also reaches close to the highest nose-down pitching moment value as can be seen from Fig. 4.1b.

5. Generation of a counter-rotating vortex at the trailing edge (α (URANS) = 19.53° and α (DES) = 19.92°) $\uparrow$: After the dynamic stall point, the DSV starts to detach from the airfoil surface and a rapid drop in C_l is observed. As the airfoil continues in upstroke, a counter-rotating vortex is formed at the trailing edge. The formation of the counter-rotating vortex can be clearly seen with the positive z-vorticity at the trailing edge in Figs. 4.6c and 4.6d. The DSV and the counter-rotating vortex can be seen in the C_p contour plots in Figs. 4.6a and 4.6b. It can also be observed that the intensity of the counter-rotating vortex captured in URANS is higher than in DES. The DSV and the counter rotating-vortex is also clearly shown in coefficient of friction plots in Figs. 4.6e and 4.6f, where the DSV can be seen as negative C_f between 0.6c and 0.8c, and the trailing edge counter rotating vortex can be seen

at 0.9c with a large positive C_f. The counter-rotating vortex leads to a slight increase in lift which can be seen as a small plateau at point 4 in the lift curve in Fig. 4.1a. This simultaneously leads to a momentary increase in the pitching moment after which it again drops (see Fig. 4.1b). This counter-rotating vortex wraps itself around the trailing edge and convects downstream while simultaneously pushing the DSV further downstream.

6. Massive separation (α (URANS) = 21.06° and α (DES) = 21.11°) $\uparrow$: At this point, a fully separated flow is observed on the suction side of the airfoil. The DSV and the counter rotating vortex detach from the trailing edge and leave the airfoil surface. Due to a decrease in lift, the negative pitching moment coefficient increases at point 6 in Figs. 4.1a and 4.1b. The C_p (Figs. 4.7a and 4.7b) and z-vorticity (Figs. 4.7c and 4.7d) contour plots show the counter-rotating vortex convecting past the airfoil trailing edge. The location of the counter-rotating vortex can be observed near the trailing edge in Figs. 4.7e and 4.7f.

7. Formation and convection of the secondary vortex (α (URANS) = 22.79° and α (DES) = 23.8°) $\uparrow$: The airfoil still continues the upstroke after the detachment of the DSV. After the DSV completely detaches from the trailing edge, the airfoil undergoes stall for a small period, and a relatively weaker secondary vortex forms and convects downstream as indicated by a relatively lower C_p region of the vortex in Figs. 4.8a and 4.8b. The spread of this secondary vortex can be seen by the z-vorticity in Figs. 4.8c and 4.8d. This secondary vortex creates a slight increase in the lift coefficient as shown by point 6 in 4.1. The location of this secondary vortex can be clearly determined by negative C_f values in the Figs. 4.8e and 4.8f.

   After this point, several simultaneous pairs of peaks and troughs are observed (see Fig. 4.1a and 4.1b) because of the formation of a series of smaller vortices which give a slight rise in lift coefficient and negative pitching moment coefficient while convecting downstream one by one. The airfoil reaches the end of the upstroke and the maximum angle of attack is reached (α = 25°) and enters the down-stroke. A total of 11 smaller vortices are observed in the URANS simulations in each cycle, excluding the DSV and the secondary vortex. They are observed

from the upstroke angle of 23.93° and down-stroke angle of 8.03°. In the DES simulations, a total of 8 vortices are observed excluding the DSV and secondary vortex from the upstroke angle of 24.18° till 8.54° in down-stroke. These smaller vortices can be identified by the crests and troughs in the Fig. 4.1a, where the crest represents the slight increase in lift coefficient due to the passing of the each vortex over the airfoil surface and the simultaneous troughs represent the convection of each vortex past the trailing edge. This formation of a series of vortices does not happen if the f is large, in which case the pitch rate is too fast to capture this phenomenon [21]. This is only specific to the cases with lower f values. Wang et al. [21] have done a similar study for a higher f value of 0.1 and this phenomenon of smaller vortices not being seen in hight f cases, can be seen in their results. These vortices have a stochastic nature in reality, so an ensemble average will not show them which is why the experimental plots do not show these vortices as they are an average of a 100 cycles.

8. Fully attached flow (α (URANS) = 7.28° and α (DES) = 6.83°) $\downarrow$: As the airfoil is undergoing down-stroke, at the end of the series of vortices, the flow starts to reattach itself from the leading edge to the trailing edge over the top surface of the airfoil. The flow becomes fully attached at this point. This can be seen from Figs. 4.9a and 4.9b, where the C_f value is entirely positive for the suction side of the airfoil showing that the flow is completely reattached.

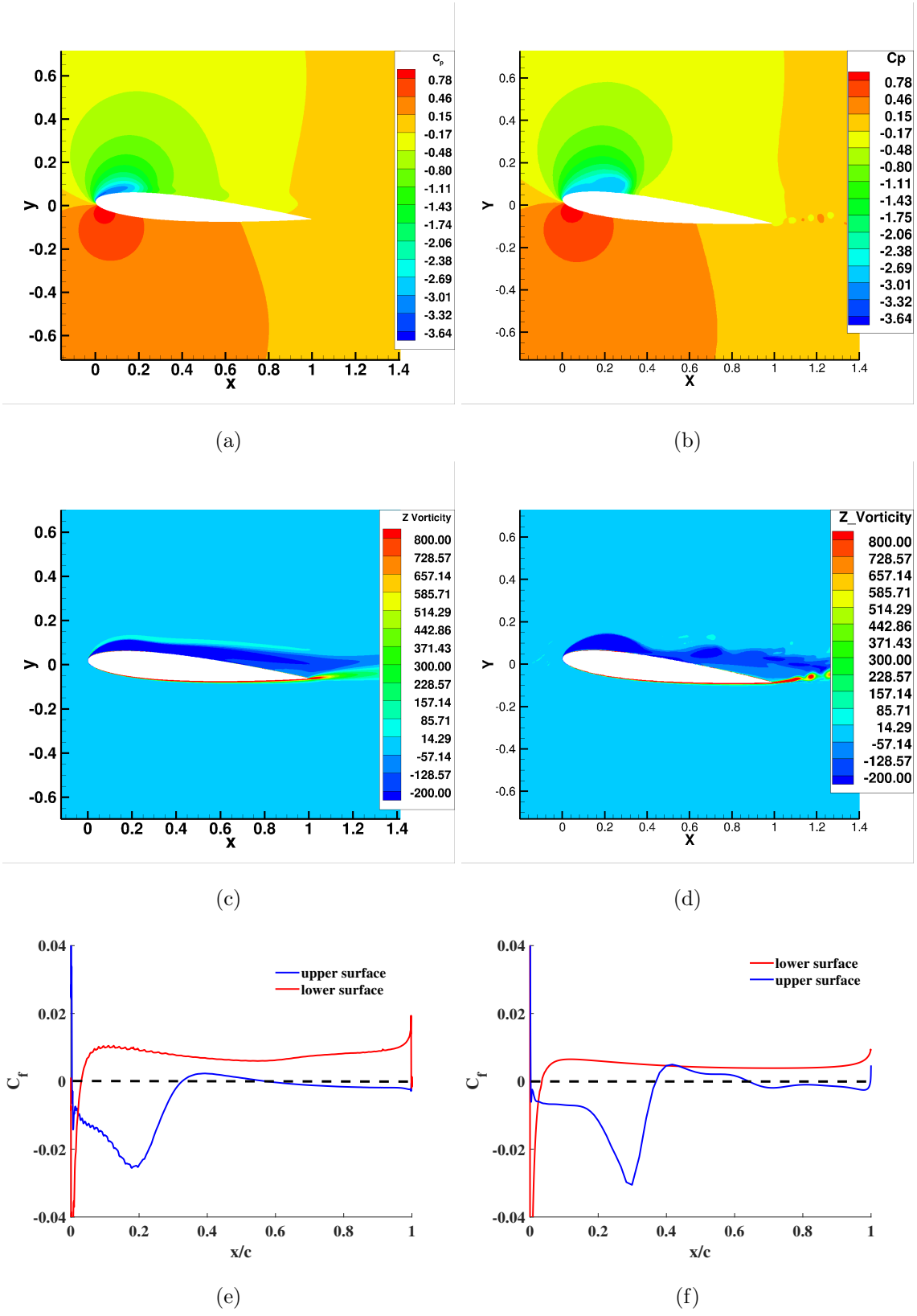

Figure 4.4: Contours for the URANS model at 15.91° ↑ of (a) pressure coefficient (C_p) curve, (c) vorticity in z-direction and (e) the C_f curve. Contours for the DES model at 17.06° ↑ of (b) C_p curve, (d) vorticity in z-direction and (f) the C_f curve.

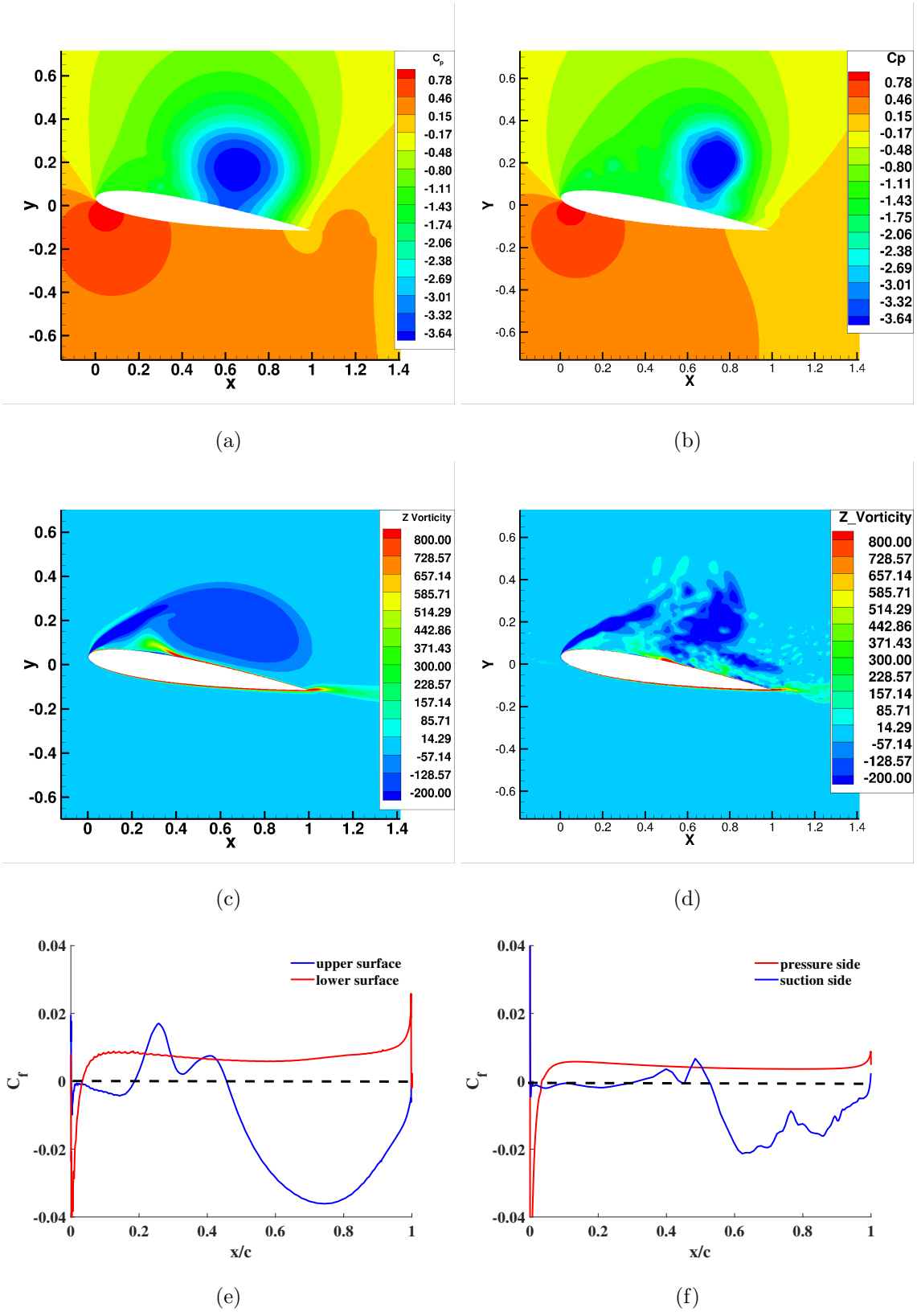

Figure 4.5: Contours for the URANS model at 18.66° ↑ of (a) C_p curve, (c) vorticity in z-direction and (e) the C_f curve. Contours for the DES model at 19.13° ↑ of (b) C_p curve, (d) vorticity in z-direction and (f) the C_f curve.

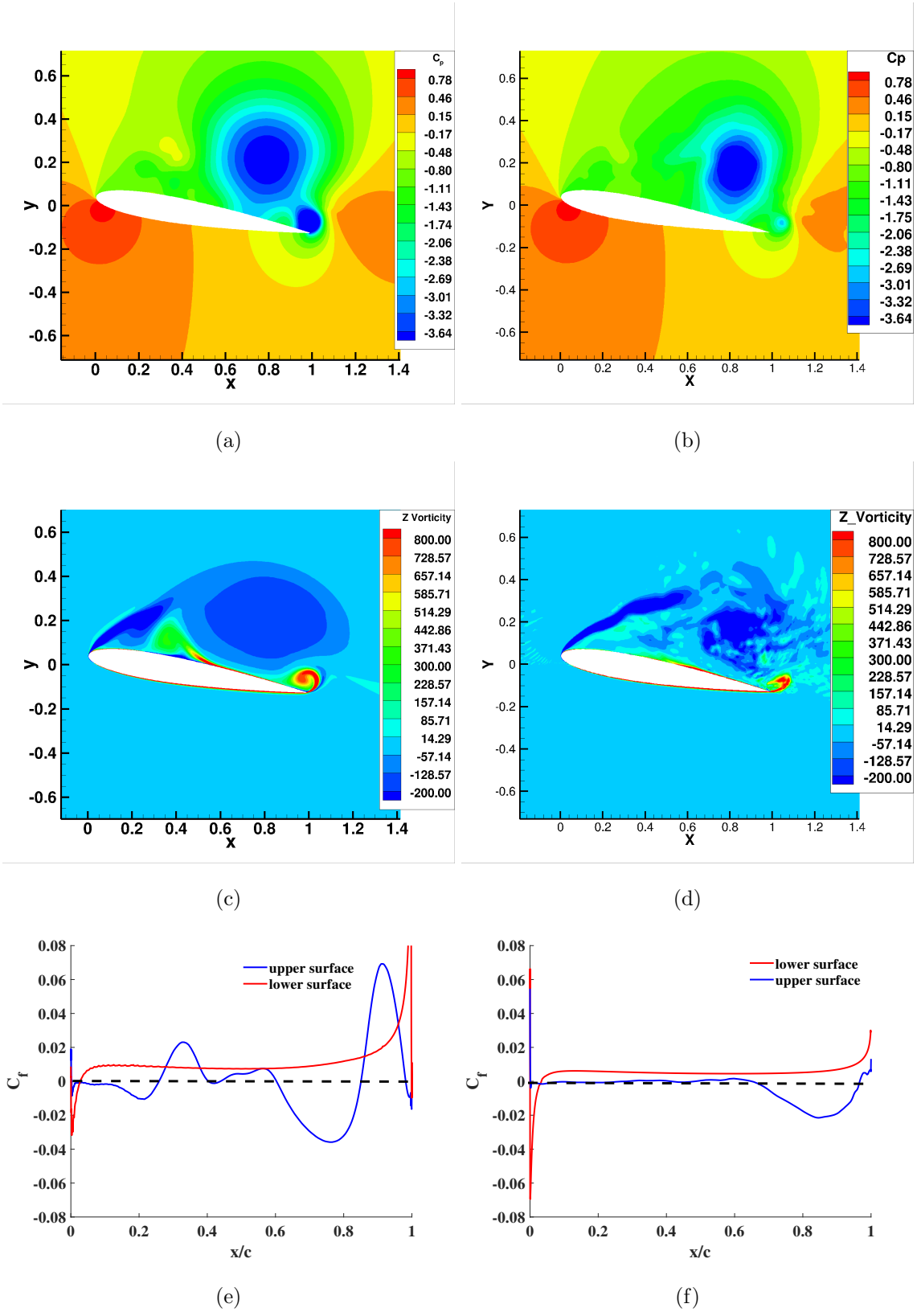

Figure 4.6: Contours for the URANS model at 19.53° ↑ of (a) C_p curve, (c) vorticity in z-direction and (e) the C_f curve. Contours for the DES model at 19.92° ↑ of (b) C_p curve, (d) vorticity in z-direction and (f) the C_f curve.

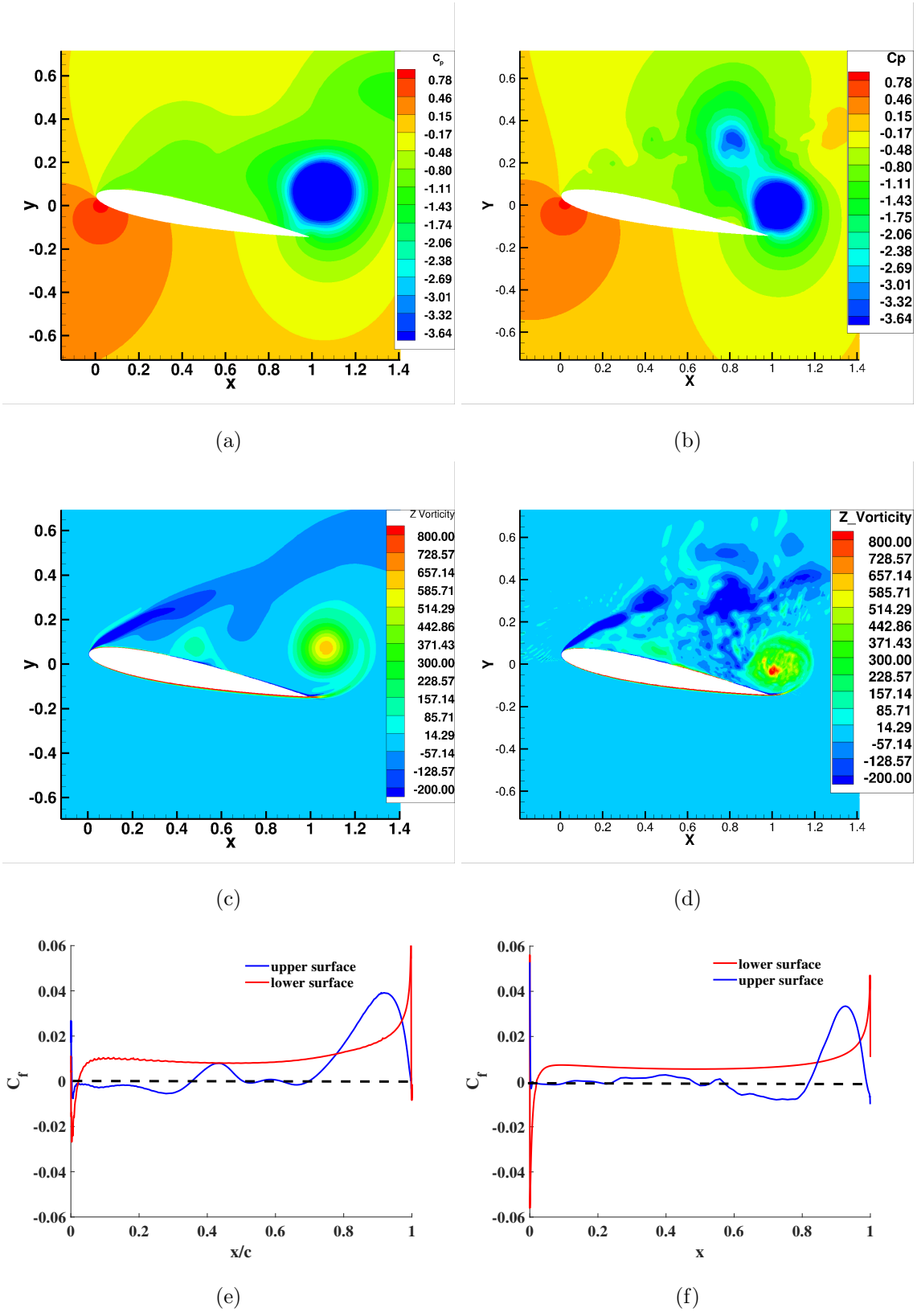

Figure 4.7: Contours for the URANS model at 21.06° ↑ of (a) C_p curve, (c) vorticity in z-direction and (e) the C_f curve. Contours for the DES model at 21.11° ↑ of (b) C_p curve, (d) vorticity in z-direction and (f) the C_f curve.

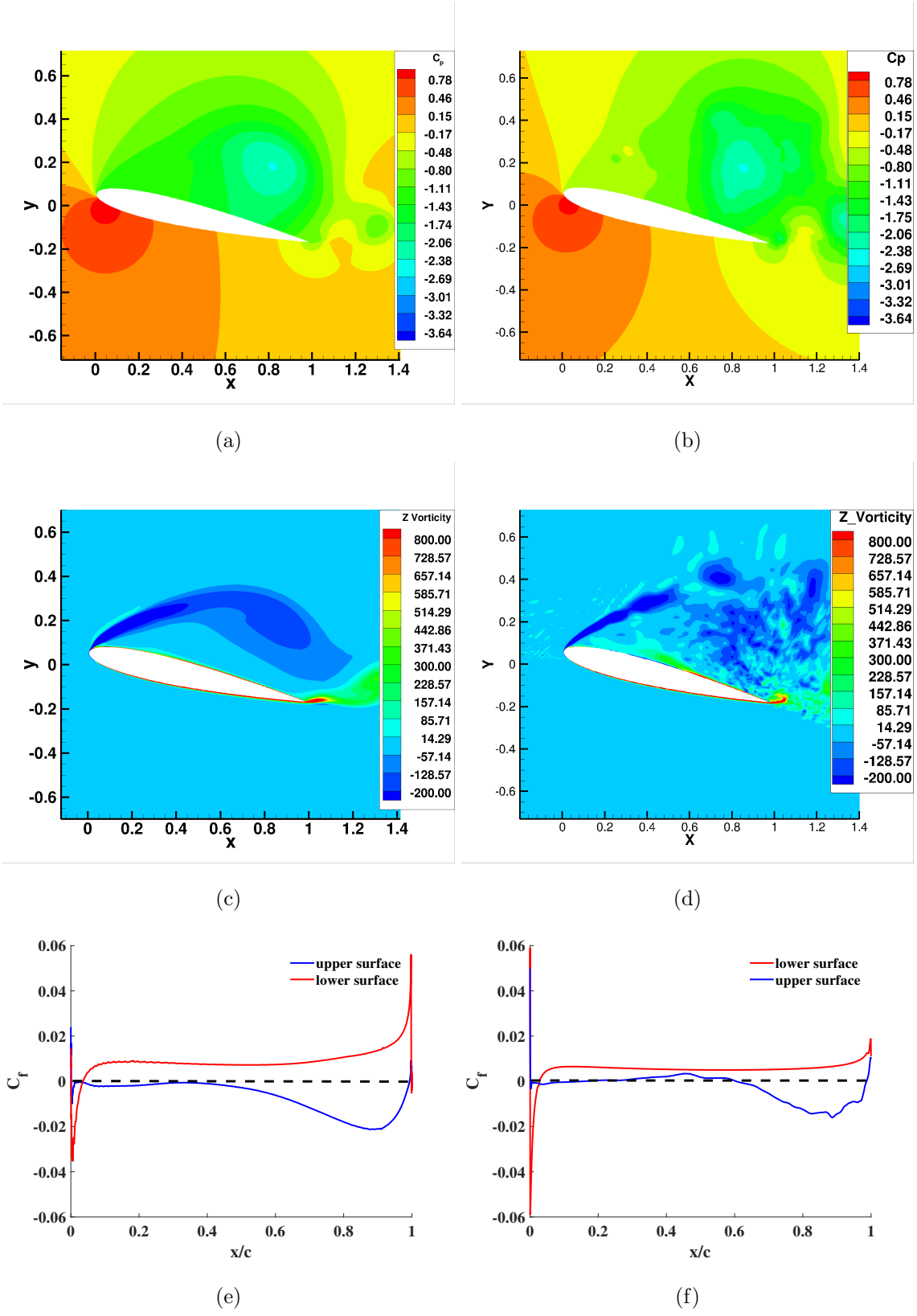

(a) (b)

(c) (d)

(e) (f)

Figure 4.8: Contours for the URANS model at 22.79° ↑ of (a) C_p curve, (c) vorticity in z-direction and (e) the C_f curve. Contours for the DES model at 23.93° ↑ of (b) C_p curve, (d) vorticity in z-direction and (f) the C_f curve.

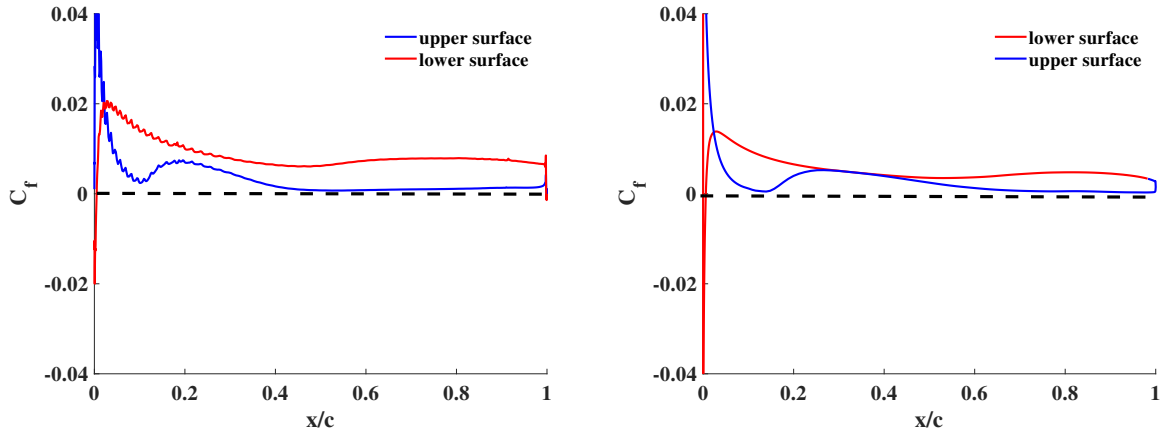

(a) (b)

Figure 4.9: Coefficient of friction plot for (a) URANS at $\alpha = 7.28° \downarrow$ and (b) DES at $\alpha = 6.83° \downarrow$ in down-stroke showing fully reattached flow

4.3 Comparison of URANS and DES with other models

The results for the $\alpha = 10°{+}15°\ sin\Omega t$ and $f = 0.05$ case are compared between the URANS, DES, LES [18] and the experiments. The LES simulations on NACA 0012 are conducted by Yusik et al. [18] for modelling the effects of freestream turbulence for wind turbine applications.

The lift, drag and pitching moment coefficient hysteresis plots for URANS, DES, LES and experiments are shown in 4.10. The important details of the models and experiments are mentioned in Table 4.1.

Table 4.1: A comparison of unsteady characteristics for all the models

Models	Moment stall point	Dynamic Stall point	Reattachment point
URANS	15.91° ↑	18.66° ↑	7.28° ↓
DES	17.06° ↑	19.13° ↑	6.83° ↓
LES	17.79° ↑	19.70° ↑	10.2° ↓
Experiments	17.23° ↑	20.61° ↑	

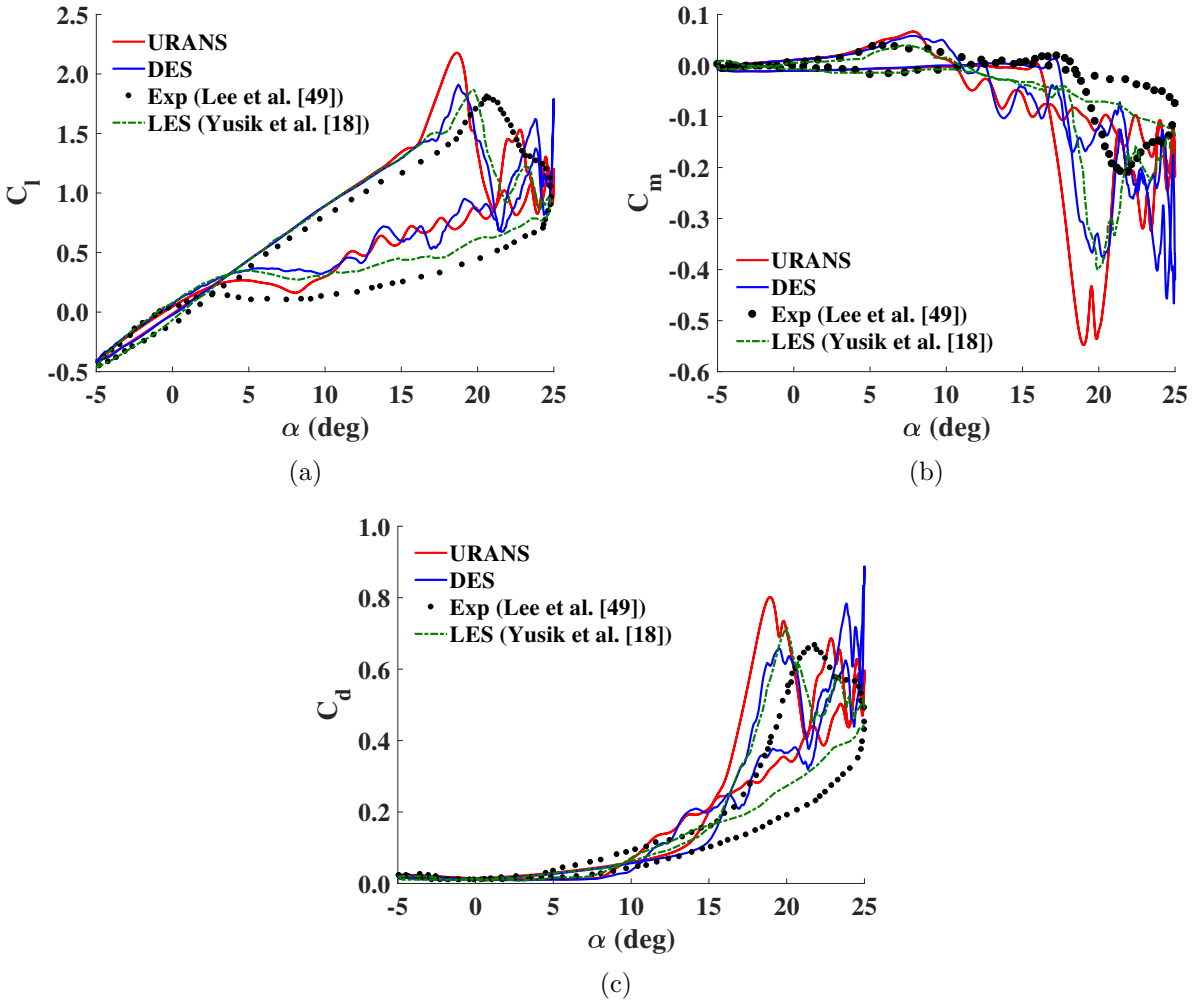

Figure 4.10: Comparison of (a) lift hysteresis plot, (b) pitching moment hysteresis plot and (c) drag hysteresis plot for URANS, DES, LES and experiments ($\alpha = 10°+15°\ sin\Omega t\ and\ f = 0.05$)

The moment stall is observed for URANS at 15.91° compared to around 17° for DES, LES and experiments. It is observed that LES captures the most delayed moment stall followed by experiments, DES and URANS. A similar trend is observed in the location of dynamic stall. The URANS captures the earliest dynamic stall, followed by DES, LES and the experiments. It is noticed that DES and LES captured similar results for the location of moment stall and dynamic stall as can be seen in table 1. It is also observed that while the URANS captured an earlier dynamic stall, it achieved a much higher peak C_l value while DES, LES and experiments showed a similar peak C_l values at the dynamic stall angle, as can be seen from Fig. 4.10a.

There is a large difference observed in the maximum negative pitching moment values captured by the simulations and the experiments. The maximum negative pitching moment is captured by URANS. The LES and DES showed similar values while the experiments showed the lowest maximum negative pitching moment values (Fig. 4.10b). The secondary vortex can be clearly seen in the URANS and DES plots by the second peak in lift coefficient plots in Fig. 4.10a. This phenomenon is also observed in the LES results by a smaller second peak in lift hysteresis plot. A secondary vortex can also be observed in the experimental results by a small plateau region from 23° to 25°.

A series of smaller vortices are captured clearly by the URANS and DES simulations and can be seen from the fluctuations observed in the C_l, C_d and C_m plots in the down-stroke pitch cycle (Fig. 4.10). These fluctuations can't be seen in the experiments which can be due to the fact that the experimental results were averaged over 100 cycles as compared to the LES (averaged over 3 cycles) and DES (averaged over 2 cycles). Another reason is that the experimental, DES and LES results are stochastic in nature whereas URANS is deterministic in nature.

As the airfoil continues in down-stroke, similar reattachment point is observed (around 7°) in URANS and DES simulations. The LES results indicated the earliest reattachment at 10.2° [18]. The time duration for 3 cycles of URANS simulations was 14,000 CPU hours whereas, 2 cycles of DES simulations took around 350,000 CPU hours while using HPC. This clearly shows that DES simulations are much more expensive than URANS simulations and there is a need for an efficient model that can reduce the vast computational resources required and the time taken for the simulations.

CHAPTER 5. CONCLUSION

In this work, URANS and DES CFD models are used to simulate the sinusoidally pitching motion in an unsteady flow over NACA 0012 airfoil at a Reynolds number 135,000. This Reynolds number regime is similar to the flow associated with small to medium sized wind turbines. The unsteady flow structure around the airfoil and the events associated with dynamic stall are studied. A comprehensive comparison of URANS, DES, LES and experimental results is conducted for low reduced frequency and deep stall case. The observations from the various unsteady events associated with dynamic stall in a pitching cycle revealed various characteristics of the lift and pitching moment hysteresis loop such as the correlation of lift curve and the development of DSV and the formation of a series of vortices. The results show there is a strong agreement between the DES and URANS results in capturing the dynamic stall events. But it is observed that both the models predicted an earlier stall value than the experiments and over predicted the peak of the lift coefficient than the experiments.

It is clear that further analysis is required to accurately predict the dynamic stall and the unsteady aerodynamic loads over an airfoil. Due to the fact that CFD simulations for accurately modeling the unsteady flow characteristics are computationally expensive, the main contribution of this thesis is the comparison study of unsteady fluid flow simulation models and to create a foundation for future multi-fidelity modeling using surrogate-based optimization approaches. Using this comparison study, it will be possible to produce an efficient multi-fidelity model which can optimize the computational resources required and reduce the overall time taken for design of dynamic-stall-resistant aerodynamic surfaces.

BIBLIOGRAPHY

[1] Eastman N Jacobs and Albert Sherman. Airfoil section characteristics as affected by variations of the reynolds number. *NACA TN 586*, 1937.

[2] Norman D Ham and Melvin S Garelick. Dynamic stall considerations in helicopter rotors. *Journal of the American Helicopter Society*, 13(2):49–55, 1968.

[3] J Gordon Leishman and TS Beddoes. A semi-empirical model for dynamic stall. *Journal of the American Helicopter society*, 34(3):3–17, 1989.

[4] Jesper Winther Larsen, Søren RK Nielsen, and Steen Krenk. Dynamic stall model for wind turbine airfoils. *Journal of Fluids and Structures*, 23(7):959–982, 2007.

[5] CJ Simao Ferreira, H Bijl, G Van Bussel, and G Van Kuik. Simulating dynamic stall in a 2d vawt: modeling strategy, verification and validation with particle image velocimetry data. In *Journal of Physics: conference series*, volume 75, page 012023. IOP Publishing, 2007.

[6] JM Martin, RW Empey, WJ McCroskey, and FX Caradonna. An experimental analysis of dynamic stall on an oscillating airfoil. *Journal of the American Helicopter Society*, 19(1):26–32, 1974.

[7] Jay M Brandon. Dynamic stall effects and applications to high performance aircraft. *NASA Langley Research Center: Hampton, Virginia*, 2(776):1–15, 1991.

[8] Philippe Wernert, Wolfgang Geissler, Markus Raffel, and Juergen Kompenhans. Experimental and numerical investigations of dynamic stall on a pitching airfoil. *AIAA Journal*, 34(5):982–989, 1996.

[9] Lars E Ericsson and J Peter Reding. Dynamic stall of helicopter blades. *Journal of the American Helicopter Society*, 17(1):11–19, 1972.

[10] Wayne Johnson. The response and airloading of helicopter rotor blades due to dynamic stall. *Massachusetts Inst of Tech Cambridge Aeroelastic and Structures Lab*, (130-1), 1970.

[11] Lawrence W Carr, Kenneth W McAlister, and William J McCroskey. Analysis of the development of dynamic stall based on oscillating airfoil experiments. *NASA TN*, (D-8382), 1977.

[12] Kenneth W McAlister, Lawrence W Carr, and William J McCroskey. Dynamic stall experiments on the naca 0012 airfoil. *NASA TP*, (1100), 1978.

[13] William J McCroskey, Kenneth W McAlister, Laurence W Carr, and SL Pucci. An experimental study of dynamic stall on advanced airfoil sections. volume 1. summary of the experiment. *NASA TM*, (84245), 1982.

[14] Lawrence W Carr. Progress in analysis and prediction of dynamic stall. *Journal of Aircraft*, 25(1):6–17, 1988.

[15] Santu T Gangwani. Synthesized airfoil data method for prediction of dynamic stall and unsteady airloads. *Vertica*, 8(2):93–118, 1983.

[16] Wayne Johnson. Comparison of calculated and measured helicopter rotor lateral flapping angles. *Journal of the American Helicopter Society*, 26(2):46–50, 1981.

[17] Van Khiem Truong. Prediction of helicopter rotor airloads based on physical modeling of 3-d unsteady aerodynamics. *Proceedings of the 22nd European Rotorcraft Forum*, pages 96.1–96.14, 1996.

[18] Yusik Kim and Zheng-Tong Xie. Modelling the effect of freestream turbulence on dynamic stall of wind turbine blades. *Computers & Fluids*, 129:53–66, 2016.

[19] Akiyoshi Iida, Keiichi Kato, and Akisato Mizuno. Numerical simulation of unsteady flow and aerodynamic performance of vertical axis wind turbines with les. In *16th Australasian Fluid*

Mechanics Conference (AFMC), pages 1295–1298. School of Engineering, The University of Queensland, 2007.

[20] Kobra Gharali and David A Johnson. Dynamic stall simulation of a pitching airfoil under unsteady freestream velocity. *Journal of Fluids and Structures*, 42:228–244, 2013.

[21] Shengyi Wang, Derek B Ingham, Lin Ma, Mohamed Pourkashanian, and Zhi Tao. Turbulence modeling of deep dynamic stall at relatively low reynolds number. *Journal of Fluids and Structures*, 33:191–209, 2012.

[22] R Nobile, M Vahdati, Janet Barlow, and A Mewburn-Crook. Dynamic stall for a vertical axis wind turbine in a two-dimensional study. In *World Renewable Energy Congress-Sweden; 8-13 May; 2011; Linköping; Sweden*, number 57, pages 4225–4232. Linköping University Electronic Press, 2011.

[23] Agis Spentzos, George N Barakos, Ken J Badcock, Bryan E Richards, P Wernert, Scott Schreck, and M Raffel. Investigation of three-dimensional dynamic stall using computational fluid dynamics. *AIAA Journal*, 43(5):1023–1033, 2005.

[24] Shengyi Wang, Derek B Ingham, Lin Ma, Mohamed Pourkashanian, and Zhi Tao. Numerical investigations on dynamic stall of low reynolds number flow around oscillating airfoils. *Computers & Fluids*, 39(9):1529–1541, 2010.

[25] K McLaren, S Tullis, and S Ziada. Computational fluid dynamics simulation of the aerodynamics of a high solidity, small-scale vertical axis wind turbine. *Wind Energy*, 15(3):349–361, 2012.

[26] Rosario Lanzafame, Stefano Mauro, and Michele Messina. 2d cfd modeling of h-darrieus wind turbines using a transition turbulence model. *Energy Procedia*, 45:131–140, 2014.

[27] Philippe R Spalart. Detached-eddy simulation. *Annual review of fluid mechanics*, 41:181–202, 2009.

[28] Sebastien Deck. Zonal-detached-eddy simulation of the flow around a high-lift configuration. *AIAA Journal*, 43(11):2372–2384, 2005.

[29] Debashis Basu, Awatef Hamed, and Kaushik Das. Des and hybrid rans/les models for unsteady seperated turbulent flow predictions. In *43rd AIAA Aerospace Sciences Meeting and Exhibit*, pages 503–516, 2005.

[30] I Celik, M Klein, M Freitag, and J Janicka. Assessment measures for urans/des/les: an overview with applications. *Journal of Turbulence*, (7):N48, 2006.

[31] Bowen Zhong, Frank Scheurich, Vladimir Titarev, and Dimitris Drikakis. Turbulent flow simulations around a multi-element airfoil using urans, des, and iles approaches. In *19th AIAA Computational Fluid Dynamics*, pages 3799–3813. 2009.

[32] Olivier Pironneau. On optimum design in fluid mechanics. *Journal of Fluid Mechanics*, 64(1):97–110, 1974.

[33] Antony Jameson. Aerodynamic design via control theory. *Journal of Scientific Computing*, 3(3):233–260, 1988.

[34] Kyriakos C Giannakoglou and Dimitrios I Papadimitriou. Adjoint methods for shape optimization. In *Optimization and Computational Fluid Dynamics*, pages 79–108. Springer, 2008.

[35] Charles A Mader and Joaquim R RA Martins. Derivatives for time-spectral computational fluid dynamics using an automatic differentiation adjoint. *AIAA Journal*, 50(12):2809–2819, 2012.

[36] Timothy M Leung and David W Zingg. Aerodynamic shape optimization of wings using a parallel newton-krylov approach. *AIAA Journal*, 50(3):540–550, 2012.

[37] Nestor V Queipo, Raphael T Haftka, Wei Shyy, Tushar Goel, Rajkumar Vaidyanathan, and P Kevin Tucker. Surrogate-based analysis and optimization. *Progress in Aerospace Sciences*, 41(1):1–28, 2005.

[38] Alexander IJ Forrester and Andy J Keane. Recent advances in surrogate-based optimization. *Progress in Aerospace Sciences*, 45(1-3):50–79, 2009.

[39] Slawomir Koziel, David Echeverría Ciaurri, and Leifur Leifsson. Surrogate-based methods. In *Computational Optimization, Methods and Algorithms*, pages 33–59. Springer, 2011.

[40] N Alexandrov, R Lewis, C Gumbert, L Green, and P Newman. Optimization with variable-fidelity models applied to wing design. In *38th Aerospace Sciences Meeting and Exhibit*, pages 841–859, 2000.

[41] TD Robinson, MS Eldred, KE Willcox, and R Haimes. Surrogate-based optimization using multifidelity models with variable parameterization and corrected space mapping. *AIAA Journal*, 46(11):2814–2822, 2008.

[42] Z-H Han, S Görtz, and R Hain. A variable-fidelity modeling method for aero-loads prediction. In *New Results in Numerical and Experimental Fluid Mechanics vii*, pages 17–25. Springer, 2010.

[43] Zhong-Hua Han, Stefan Görtz, and Ralf Zimmermann. On improving efficiency and accuracy of variable-fidelity surrogate modeling in aero-data for loads context. In *CEAS 2009 European Air and Space Conference*. Royal Aeronautical Soc. London, 2009.

[44] Zhong-Hua Han, Ralf Zimmermann, and Stefan Goretz. A new cokriging method for variable-fidelity surrogate modeling of aerodynamic data. In *48th AIAA Aerospace Sciences Meeting Including the New Horizons Forum and Aerospace Exposition*, pages 1225–1247, 2010.

[45] Andrew March and Karen Willcox. Provably convergent multifidelity optimization algorithm not requiring high-fidelity derivatives. *AIAA Journal*, 50(5):1079–1089, 2012.

[46] Andrew March and Karen Willcox. Constrained multifidelity optimization using model calibration. *Structural and Multidisciplinary Optimization*, 46(1):93–109, 2012.

[47] D Echeverría and PW Hemker. Manifold mapping: a two-level optimization technique. *Computing and Visualization in Science*, 11(4-6):193–206, 2008.

[48] Benjamin Peherstorfer, Karen Willcox, and Max Gunzburger. Survey of multifidelity methods in uncertainty propagation, inference, and optimization. *SIAM Review*, 60(3):550–591, 2018.

[49] T Lee and P Gerontakos. Investigation of flow over an oscillating airfoil. *Journal of Fluid Mechanics*, 512:313–341, 2004.

[50] Jaber AlMutairi, Eltayeb ElJack, and Ibraheem AlQadi. Dynamics of laminar separation bubble over naca-0012 airfoil near stall conditions. *Aerospace Science and Technology*, 68:193–203, 2017.

[51] Jurij Sodja. Turbulence models in cfd. *University of Ljubljana*, pages 1–18, 2007.

[52] Florian R Menter. Two-equation eddy-viscosity turbulence models for engineering applications. *AIAA Journal*, 32(8):1598–1605, 1994.

[53] Francisco Palacios, Juan Alonso, Karthikeyan Duraisamy, Michael Colonno, Jason Hicken, Aniket Aranake, Alejandro Campos, Sean Copeland, Thomas Economon, Amrita Lonkar, et al. Stanford university unstructured (su 2): an open-source integrated computational environment for multi-physics simulation and design. In *51st AIAA Aerospace Sciences Meeting including the New Horizons Forum and Aerospace Exposition*, pages 287–347, 2013.

[54] Eiji Shima, Keiichi Kitamura, and Takanori Haga. Green–gauss/weighted-least-squares hybrid gradient reconstruction for arbitrary polyhedra unstructured grids. *AIAA Journal*, 51(11):2740–2747, 2013.

[55] Youcef Saad. A flexible inner-outer preconditioned gmres algorithm. *SIAM Journal on Scientific Computing*, 14(2):461–469, 1993.

[56] Seokkwan Yoon and Antony Jameson. Lower-upper symmetric-gauss-seidel method for the euler and navier-stokes equations. *AIAA Journal*, 26(9):1025–1026, 1988.

[57] Antony Jameson. Origins and further development of the jameson–schmidt–turkel scheme. *AIAA Journal*, pages 1487–1510, 2017.

[58] Venkat Venkatakrishnan. On the accuracy of limiters and convergence to steady state solutions. *AIAA Journal*, pages 880–890, 1993.

[59] S Venkateswaran and Charles Merkle. Dual time-stepping and preconditioning for unsteady computations. *AIAA Journal Paper 95-0078*, pages 1–14, 1995.

[60] PR Eiseman and K Rajagopalan. Automatic topology generation. In *New Developments in Computational Fluid Dynamics*, pages 112–124. Springer, 2005.

[61] Philippe R Spalart and Craig Streett. Young-person's guide to detached-eddy simulation grids. *NASA, Technical Report CR-2001-211032*, 2001.

[62] Philippe R Spalart. Comments on the feasibility of les for wings, and on a hybrid rans/les approach. In *Proceedings of First AFOSR International Conference on DNS/LES*. Greyden Press, 1997.

[63] Zifei Yin, KR Reddy, and Paul A Durbin. On the dynamic computation of the model constant in delayed detached eddy simulation. *Physics of Fluids*, 27(2):025105, 2015.